Ligand Substitution Effect on Electronic Structure and Optical Properties of Nickel Porphyrazines

Liqun Guo,[†,§] **D. E. Ellis,***[†,‡] **B. M. Hoffman,**[‡,§] **and Y. Ishikawa**[||]

Departments of Physics and Chemistry and Materials Research Center, Northwestern University,
Evanston, Illinois 60208, and Department of Applied Chemistry, Oita University,
Dannoharu, Oita 870-11, Japan

Received January 5, 1996[⊗]

Self-consistent density functional calculations have been performed on a variety of planar conjugated Ni-centered macrocycles with a basic porphyrazine (tetraazaporphyrin) core and peripheral dithiolene groups (PZ) or fused-benzo groups (PC). Theoretical energy level diagrams, charge distributions, and densities of states have been obtained in order to understand the electronic structure modifications due to peripheral ligand substitution. The substituents role in altering electronic properties and charge distribution of the porphyrazine macrocycles has been used to interpret the observed variations in optical absorption profiles. In the Q-band (∼680 nm) region, a single peak is seen for high symmetry (D_{4h}) macrocycles and a double peak for lower symmetry (D_{2h} and C_{2v}) systems. Calculated intensities and band splittings are compared in detail with qualitative molecular orbital models and experiment in the visible and UV regions. Predictions are made for the infrared absorption and semiconducting band gap.

I. Introduction

Porphyrinic conjugated macrocycles have been a subject of great interest due to the high synthetic possibilities, rich coordination chemistry, numerous technological applications, and biological importance. The physical properties of these square planar porphyrin-like molecules depend strongly on their chemical and geometric structure, providing an enormous opportunity for molecular design and control of properties by ligand substitution and ring symmetry modification. Porphyrazines and related molecules have also been a theme of considerable theoretical interest due to their high symmetry, planar atomic arrangements, and electronic delocalization. A large number of theoretical works have been devoted to the understanding of the atomic scale structure of these molecules, their building blocks, and the mechanisms of charge transport and optical properties.[1,2] Molecular design of porphyrazines for various Q-band splitting modes has attracted considerable experimental interest, where the ring symmetry modification has been introduced as a new methodology.[3] Our theoretical investigations aim to provide insight into the microscopic origins of the behavior of these molecules based on the relationship between their chemical and electronic properties. We have performed self-consistent density functional electronic structure calculations for a number of macrocycles with basic porphyrazine structure and peripherally fused-benzo rings (PC) and dithiolene groups (PZ). These molecules show electronic absorption in the visible region (Q-band, ca. 680 nm), with band-splitting and shifts linked to overall symmetry and composition of the macrocycles. A single peak is observed for 4PZ and 4PC high symmetry (D_{4h}) macrocycles. Ligand substitution leads to the splitting of the Q-band into two peaks in the 2 PC/2 PZ cis, 3 PC/1 PZ, 1 PC/3 PZ (C_{2v}), and 2 PC/2 PZ trans (D_{2h}) configurations. Calculated intensities and band splittings are compared in detail with qualitative molecular orbital models and experiments in the visible (Q- and B-bands) and UV. Theoretical energy level diagrams, partial densities of states, effective electronic configurations, and charge distributions in these macrocycles are obtained to explain the electronic influence of the peripheral ligands on the porphyrazine “core”.

II. Theoretical Model

A. Local Density Functional DV Method. In this work electronic structure calculations are performed using the first principles density functional (DF) theory. Single particle orbitals are obtained using the discrete variational (DV) method.[4−7] The Hamiltonian consists of the sum of a kinetic energy operator, nuclear and electronic Coulomb potentials, and an exchange and correlation potential. Eigenfunctions of the effective Hamiltonian are expanded in a basis of numerical atomic orbitals, and the potential is iterated to self-consistency.

Numerical free-atom basis functions $\{A_j\}$ are used to obtain the molecular eigenfunctions as a linear combination of atomic orbitals (LCAO)

$$\psi_i(\vec{r}) = \sum_j A_j(\vec{r})C_{ji} \tag{1}$$

The atomic populations and related partial densities of states can be used to develop a detailed chemically appealing description of the local atomic environment.

In the nonrelativistic approach, the density of electrons of spin component $s_z = \sigma$ is

$$\rho_\sigma(\vec{r}) = \sum_i n_{i\sigma}|\psi_{i\sigma}(\vec{r})|^2 \tag{2}$$

where $n_{i\sigma}$ are the occupation numbers which are chosen for the ground state according to Fermi−Dirac statistics, and ψ_i are the single particle orbitals which are self-consistently generated. The charge density is given by $\rho_C = \rho\!\uparrow + \rho\!\downarrow$.

[†] Department of Physics, Northwestern University.

[‡] Department of Chemistry, Northwestern University.

[§] Materials Research Center, Northwestern University.

[||] Oita University.

[⊗] Abstract published in *Advance ACS Abstracts,* August 1, 1996.

(1) Liang, X. L.; Flores, S.; Ellis, D. E.; Hoffman, B. M.; Musselman, R. L. *J. Chem. Phys.* **1991**, *95*, 403 and references therein.

(2) Liang, X. L.; Ellis, D. E.; Gubanova, O. V.; Hoffman, B. M. *Int. J. Quantum Chem*. **1994**, *52*, 657.

(3) Ishikawa, Y.; Hoffman, B. M. Unpublished work.

(4) Ellis, D. E.; Painter, G. S. *Phys. Rev. B* **1970**, *2*, 2887.

(5) Baerends, E. J.; Ellis, D. E.; Ros, P. *J. Chem. Phys.* **1973**, *2*, 40.

(6) Rosen, A.; Ellis, D. E.; Adachi, H.; Averill, F. W. *J. Chem. Phys.* **1976**, *65*, 3629.

(7) Delley, B.; Ellis, D. E. *J. Chem. Phys.* **1982**, *76*, 1949.

S0020-1669(96)00005-5 CCC: $12.00

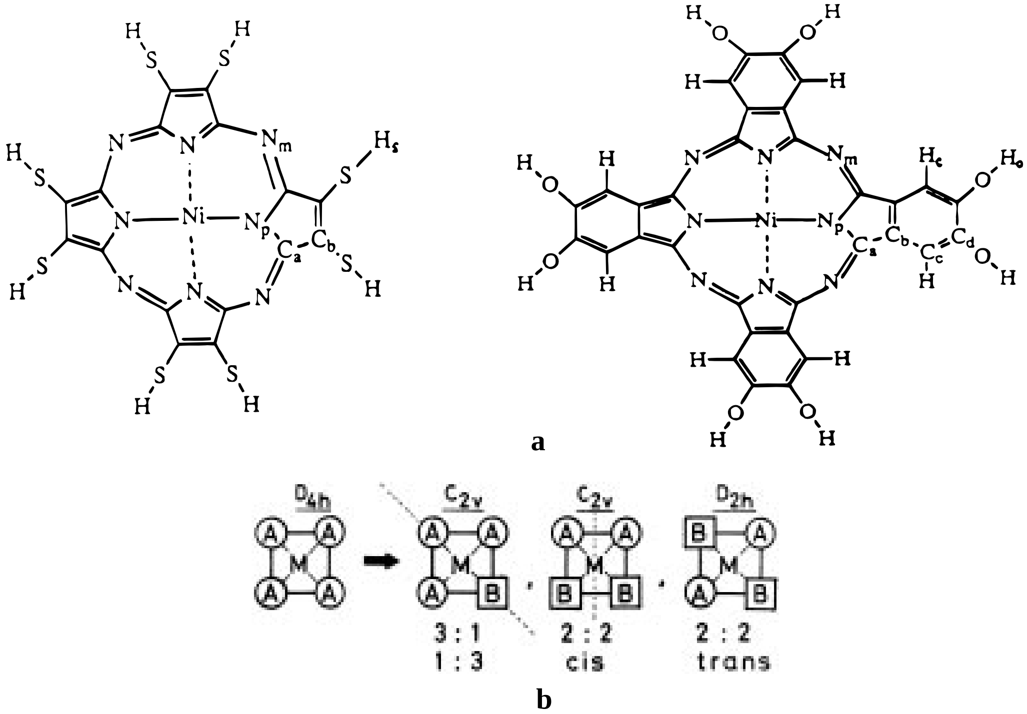

Figure 1. (a) D_{4h} basic structure. (b) Peripheral ligand substitutions.

In order to solve the Poisson equation for the Coulomb potential efficiently, ρ_C is fitted to a multipolar expansion basis. The simplest so-called self-consistent-charge (SCC) scheme[6] is based upon Mulliken population analysis of orbital densities, which gives a familiar and intuitive picture of effective atomic configurations. The extension of the fit by least squares self-consistent-multipolar (SCM) methods can be carried to any desired level of precision.[7] The von Barth−Hedin exchange-correlation potential[8] and the SCM expansion are used in the present work.

B. Density of States. The energy spectrum of valence eigenfunctions is best displayed as an energy-dependent density of states. The contribution of state nl of atom υ to the DOS is represented by[9]

$$D^{\nu}_{nl}(E) = \sum_{p} f^{\nu}_{nl,p} L(E - \epsilon_p,\sigma) \tag{3}$$

where $f_{nl,p}$ is the appropriate Mulliken population[10] contribution to the pth molecular orbital. $L(E - \epsilon_p,\sigma)$ is a line shape function chosen as a Lorentzian of width σ, which is defined in eq 4. By summing all partial DOSs (PDOSs), we obtain the total DOS.

$$L(E - \epsilon_p,\sigma) = \frac{\sigma/\pi}{(E - \epsilon_p)^2 + \sigma^2} \tag{4}$$

C. Optical Properties. The theoretical optical absorption spectrum can be defined as

$$I(\epsilon) = \sum_{\mathrm{i,f}} L(\epsilon - \epsilon_{\mathrm{if}},\sigma) n_{\mathrm{i}}(1 - n_{\mathrm{f}}) f(\epsilon_{\mathrm{if}}) \tag{5}$$

where $L(\epsilon - \epsilon_{\mathrm{if}},\sigma)$ is defined as in eq 4 and n_{i} and n_{f} are initial and final state occupation numbers, respectively. The summation in eq 5 is limited to initial and final states whose symmetry product $\gamma_i \times \gamma_j$ permits dipole absorption.

The dipole matrix elements $\langle \psi_{\mathrm{f}}|\mathbf{r}\cdot\hat{\mathbf{e}}|\psi_{\mathrm{i}}\rangle$ are calculated by direct integration over initial and final state wave functions to get polarized absorption profiles. The oscillator strength $f(\epsilon_{\mathrm{if}})$ is defined as

$$f(\epsilon_{\mathrm{if}},\hat{\boldsymbol{e}}) = \frac{2m}{\hbar^2}\epsilon_{\mathrm{if}}|\langle \Psi_{\mathrm{f}}|\vec{\boldsymbol{r}}\cdot\hat{\boldsymbol{e}}|\Psi_{\mathrm{i}}\rangle|^2 \tag{6}$$

where ϵ_{if} is the transition energy, and $\hat{\mathbf{e}}$ is the unit wavevector of incident light.

In density functional theory, orbital energies are not in general directly connected with excitation energies of the system. However, long experience has shown that under many circumstances, dictated by the degree of localization of initial and final states, orbital energy differences $\epsilon_{\mathrm{f}} - \epsilon_{\mathrm{i}}$ can give a good approximation to the excitation energies ϵ_{if}. When optical transitions of interest connect the occupied and the lower-lying excited states, all of which are of rather diffuse character, there is little change in the potential and we may use molecular orbitals generated from the ground state potential as both initial ($|\psi_{\mathrm{i}}\rangle$) and final ($|\psi_{\mathrm{f}}\rangle$) states in a reasonable approximation.[11] The transition state procedure[12] may be used to include electronic excited state relaxation yielding a better approximation to ϵ_{if}. In the present work, we found that transition state calculations shift the optical spectrum by only 0.1−0.2 eV, so that use of ground state orbitals and energies is well justified.

III. Results

A. Geometry Modification. Molecular structure of the modified porphyrazines is shown in Figure 1; note that terminal groups have been replaced by H for simplicity. The structure can be thought of as a porphyrazine (tetraazaporphyrin) with four substituents peripherally fused. The framework of these molecules consists of carbon and nitrogen atoms in a planar arrangement with a metal (e.g. Ni) coordinated in the center. Figure 1a with four dithiolene moieties (4PZ) represents star-porphyrazine, a new polynucleating porphyrinic ligand recently synthesized by Velazquez et al.[13] The bond angles and distances for the sulfur atoms, a- and b-carbons, and meso (m) and pyrrole

---

(8) vonBarth, U.; Hedin, L. *J. Phys.* **1972**, *C5*, 1629.

(9) Press, M. R.; Ellis, D. E. *Phys. Rev. B* **1987**, *35*, 4438.

(10) Mulliken, R. S. *J. Chem. Phys.* **1955**, *23*, 1833.

(11) See for example: *Density Functional Theory of Molecules, Clusters, and Solids*; Ellis, D. E., Ed.; Kluwer Academic: Dordrecht, The Netherlands, 1995.

(12) Slater, J. C. *The Self-Consistent Field for Molecules and Solids*; McGraw-Hill: New York, 1974.

(13) Velazquez, C. S.; Fox, G. A.; Broderick, W. E.; Andersen, K. A.; Anderson, O. P.; Barrett, A. G. M.; Hoffman, B. M. *J. Am. Chem. Soc.* **1992**, *114*, 7416.

Table 1. Net Charge Distributions of Nickel Porphyrazines

system	orbital	4PZ	4PC	2C2Z trans	2C2Z cis	1C3Z	1Z3C
Metal Atomic Orbital Populations							
Ni							
	3d	8.30	8.20	8.22	8.21	8.31	8.28
	4s	0.07	0.16	0.09	0.06	0.08	0.04
	4p	0.16	0.19	0.14	0.15	0.18	0.18
Net Atomic Charges of TAP Core							
Ni		1.47	1.45	1.55	1.58	1.44	1.50
N_p		−0.29	−0.42	−0.25	−0.17	−0.27	−0.19
N_m		−0.11	−0.25	0.03	0.09	−0.06	0.02
C_a		0.04	0.07	−0.05	−0.02	0.05	−0.03
Net Atomic Charges of Peripheral Ligands							
C_b		0.13	0.05	0.10	−0.04	0.04	0.09
C_c			−0.48	−0.71	−0.60	−0.64	−0.29
C_d			0.38	0.31	0.26	0.40	0.03
O			−0.93	−0.67	−0.90	−1.21	−1.16
S		−0.84		−0.98	−0.69	−0.78	−0.73
H_o			0.78	0.71	0.68	0.85	0.85
H_s		0.68		0.67	0.47	0.65	0.57
H_c			0.28	0.50	0.63	0.44	0.51

(p) nitrogens were taken from X-ray crystallographic data and symmetry-averaged to allow D_{4h} symmetry (in good approximation) of the molecule. Introducing a second ring component causes symmetry reduction in the macrocycle (Figure 1b) and leads to modified spectral features. Keeping the star-porphyrazine core unchanged, we reduce the high symmetry star-porphyrazine ("4 PZ") and phthalocyanine ("4 PC") to D_{2h} (2C2Z trans) or C_{2v} (2C2Z cis, 1C3Z, 1Z3C) depending upon the dithiolene and benzene groups arrangements. This may cause significant changes in the electronic structure of the entire macrocycle, revealed by their different optical properties. We focus here on the optical Q-band region, where to a first approximation one expects to see perturbations on the porphyrine "$\pi \rightarrow \pi^*$" transitions. A preliminary analysis will also be given of the higher energy charge-transfer transitions responsible for the Soret band and for absorption features special to the peripheral ligands. Terminal groups far away from the porphyrazine ring ($-(CH_2CH_2O)_3H$ in star-porphyrazine and $-(CH_2)_7CH_3$ in the phthalocyanine macrocycle) which are attached to the outer oxygen atoms have not been considered in the calculations. Instead, terminal hydrogen atoms H_o were introduced (Figure 1) to maintain the bonding coordination of exterior atoms. In order to test possible effects of H termination, calculations were also performed using methyl groups as terminators in 4PZ and 4PC cases. No significant differences in electronic structure associated with the porphyrazine region were found.

B. Electronic Structure. 1. Self-Consistent Atomic Configuration. Ligand substitution introduces significant changes at the substitution site, i.e. exterior framework carbons. However, if the interaction is of highly delocalized character, it would also be expected to weakly affect the 'core' carbon (C_a)−nitrogen (N_p, N_m) macrocycle and its coupling to the central metal (Ni). Effective electronic charges and atomic configurations are given in Table 1 for the six species 4PC, 4PZ, 2C2Z trans, 2C2Z cis, 1C3Z, and 1Z3C. It is well-known that Mulliken atomic orbital populations do not have an *absolute* significance, due to their dependence upon basis; it is also well-known that *trends* from one molecule to another are significant, and quite valuable in chemical interpretation. We wish to first draw attention to very stable features of the metal and TAP core, and then observe the subtle differences which arise from peripheral substitution. Nominally divalent, Ni is found to donate ∼1.5 e in all the macrocyles with a typical effective configuration $3d^{8.3}4s^{0.1}4p^{0.2}$ with net Mulliken charge in the range from 1.44 (1C3Z) to 1.58 e (2C2Z). The excess 0.2−0.3 3d electron is associated with covalent bonding to N, while the 4sp occupancy shows the participation of Ni in the diffuse states responsible for quasi-one-dimensional chain conductivity in partially oxidized compounds. Charge transfer to the pyrrole nitrogen is seen to range from 0.17 to 0.42 e, thus varying significantly with peripheral ligands.

Inequivalent types of meso and pyrrole nitrogens and a, b, c, and d carbons result from the local electronic structure changes as a result of the geometry modification and symmetry lowering in the macrocycle. Pyrrole nitrogen atoms are found to be considerably more electronegative than meso N, C_a, and C_b carbons become slight electron donors in case of D_{4h} symmetry 4PC or 4PZ ligands and are weak acceptors in three of the four low symmetry cases. C_c carbon atoms of the benzene rings are strong electron acceptors from the hydrogens, while C_d atoms donate electrons to the oxygens in PC ligands.

2. Density of States. Total density of states (DOS) and partial density of states (PDOS) of the Ni-centered porphyrazines are shown in Figure 2. The Fermi energy (E_F) of a molecule is defined to lie halfway between HOMO and LUMO energies, as is the case in semiconductors and insulators. In Figure 2, we choose E_F as the zero point of the energy axis. Total DOS, shown at the bottom of each panel, gives an overview of the energy level distribution similar to that of traditional energy level diagrams. The large number of states present makes a continuous curve (see eqs 3 and 4) representation most useful. The DOS can be compared directly with UV and X-ray photoelectron spectra; in practice UPS and XPS of such complex molecules are not very useful because of the large number of unresolved components. Fortunately, theory can resolve the DOS into its constituent PDOS; in principle, experimental data can be taken as a function of photon energy and polarization and partial deconvolution achieved. This has occasionally been done to extract the metal-d contribution, for example.

The atom- and state-selected partial DOS can give us a direct measure of the chemical bonding characteristics in the local environment; e.g., around the central Ni, which complements the interpretation of atomic populations. Thus we find in each case a well-defined Ni 3d "band" spanning a region 2−3 eV, and centered about 1.5 eV below E_F. The diffuse 4sp components are seen to reach as far as 6 eV below E_F, contributing to bonding stability, and extend as excited states in the optical region beginning ∼2 eV above E_F. Examining the PDOS of various species in the valence band region of 0 to −4 eV, we immediately see strong ligand orbital contributions not only from both C and N, but also from peripheral O and S in the energy region accessible for optical transitions. The overlap (in energy) between PDOS originating from these atoms, and the considerable width of these bands indicates the degree of mixing of atomic character and interaction among these atoms. These diagrams are of considerable help in understanding the optical properties as described below; here we summarize the principal features seen in PDOS of each molecule.

a. 4PZ. For the high symmetry D_{4h} 4PZ group (Figure 2a), S 3p and 3d contributions energy overlap strongly with Ni 3d states, pyrrole nitrogen 2p orbitals and carbon 2p states spanning 0−2 eV below the E_F in the valence region. Meso nitrogen 2s,2p states lie about 4−6 eV below E_F and interact strongly with a broad band of C_a and C_b 2s,2p orbitals ranging over 0−10 eV below E_F in the valence region. S 3p and 3d states also interact with C_b 2p states at ∼2eV above E_F.

b. 4PC. For the other D_{4h} group 4PC, Figure 2b, the main features of the peripheral O 2p states are shifted to lower energy(∼2−4 eV below E_F) compared to sulfur states of the 4PZ

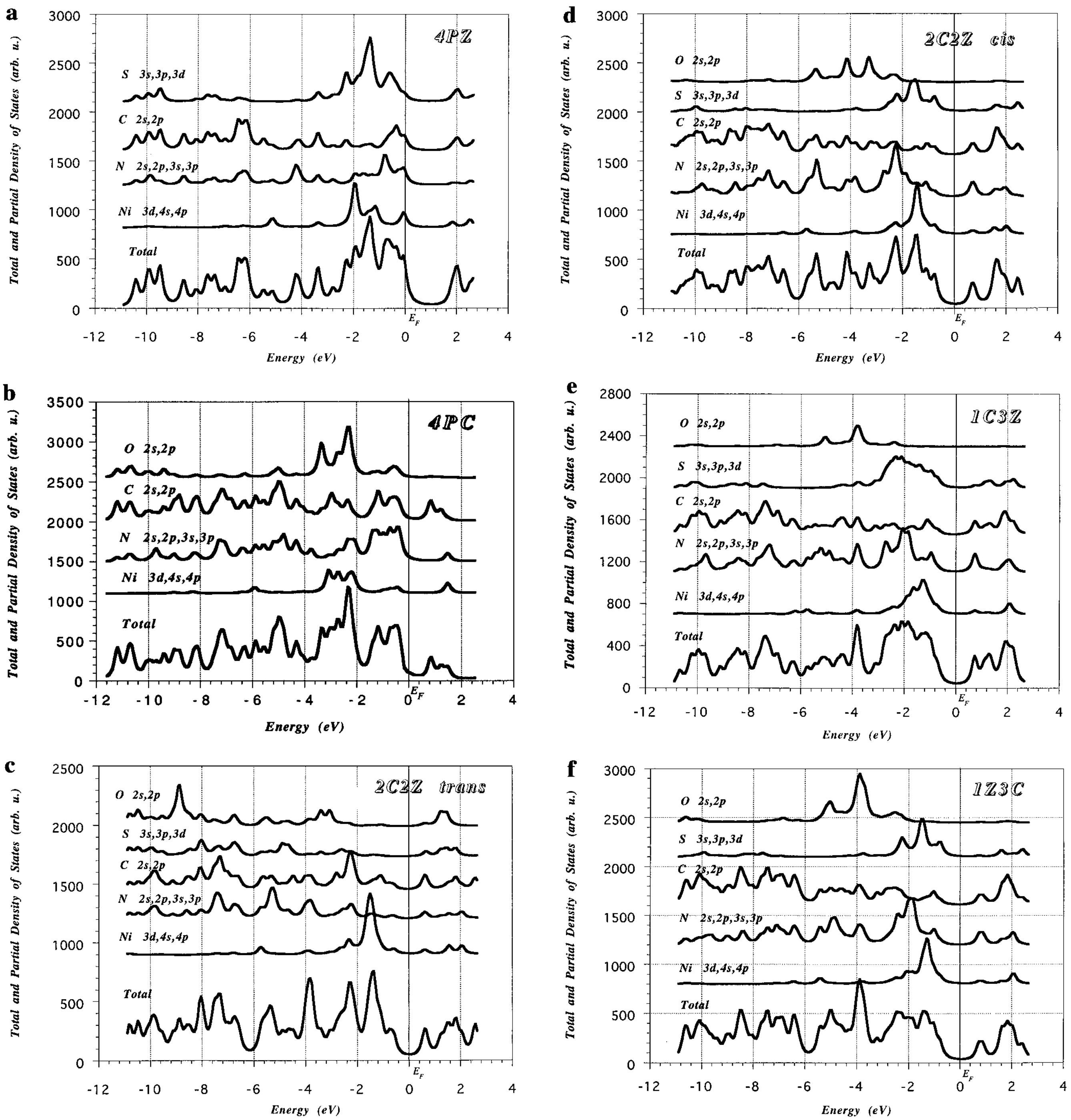

Figure 2. (a) Total and partial density of states of 4PZ. (b) Total and partial density of states of 4PC. (c) Total and partial density of states of 2C2Z trans. (d) Total and partial density of states of 2C2Z cis. (e) Total and partial density of states of 1C3Z. (f) Total and partial density of states of 1Z3C.

dithiolene groups. However, some O 2p character remains in the 0−2 eV region. The carbon PDOS is enhanced in 4PC due to the peripheral benzene ring contributions. Ni 3d states overlap and interact with N 2p states at about 2−3 eV below E_F. Carbon 2p states interact with the "core" pyrrole-N s,p orbitals and Ni 3d states at ∼1.5 eV above E_F.

c. 2C2Z trans. For the D_{2h} symmetry trans-coordinated molecule 2C2Z trans (Figure 2c), peripheral S and O bands broaden and shift significantly toward greater binding energy. Carbon and nitrogen states of the basic porphyrazine framework form a highly delocalized structure over the entire valence region. Ni 3d states remain localized at about 1−2 eV below E_F and are not much affected by the ligand substitution. Peripheral carbon C_c and C_d 2p states interact with O 2p states and S 3p,3d states over the region 0.5−2 eV above the Fermi energy.

d. 2C2Z cis. For the other 2:2 substituted C_{2v} molecule 2C2Z cis (Figure 2d), two distinct bands are formed in the upper valence region with S 3s,3p lying about 1.5 to 2.5 eV below E_F and O 2p at about 3−4 eV below E_F. Meso- and pyrrole-nitrogens interact strongly with Ni 3d at ∼1−2 eV below E_F, as in previously discussed cases. N s,p, C_a and C_b 2p, and some S 3p and O 2p states contribute to the DOS structure 1−2 eV above the Fermi energy.

e. 1C3Z. For the 1C3Z substituted C_{2v} molecule (Figure 2e), S 3p,3d and O 2s,2p states display a PDOS similar to that of 2C2Z, occupying the region 1−3 eV and 3−5 eV below E_F, respectively. Ni 3d states again span the region about 1−2 eV

Table 2. Highest Occupied Molecular Orbital (HOMO) and Lowest Unoccupied Molecular Orbital (LUMO) Energies (eV) and Atomic Orbital Contributions (%), As Calculated from Ground State Energy Levels

			Ni	N_p	N_m	C_a	C_b	C_c	C_d	S		O	H
	E_{HOMO}	E_{LUMO}	3d	2p	2p	2p	2p	2p	2p	3p	3d	2p	1s
4PZ													
$3a_{1u}$	−5.86					66	12			22			
$12b_{1g}$		−4.00	21	10		11	13			4	18		18
4PC													
$7e_g$	−5.99		8	15	36		9		15			16	
$8e_g$		−4.57		12			23		32			32	
2C2Z trans													
$8b_{3g}$	−3.71		13	8			22			54			
$9b_{2g}$		−2.53	10	14	18	29	11	5		9		1	
2C2Z cis													
$16b_1$	−2.74		15	6			24			50			
$16a_2$		−1.31	7	18	16	28	17	3	4	5		2	
1C3Z													
$14a_2$	−3.75		17	7		6	10		11	46			
$15a_2$		−2.32	7	10	24	26	21	1	3	5		1	
1Z3C													
$17b_1$	−4.59		15	7			23			51			
$15a_2$		−3.09	9	12	21	27	14	3	7	4		2	

below E_F. Carbon C_a and C_b 2p states, nitrogen 2p states, and S 3p states dominate the region 0.8−2.4 eV above the Fermi energy.

f. 1Z3C. For the 1Z3C substituted C_{2v} molecule (Figure 2f), O 2p states again fall in the region 2.5−5.0 eV below the Fermi energy, lying below S 3p,3d states at 1.0−2.2 eV below E_F. Ni 3d states are essentially unchanged, at ~1−2 eV below E_F, and N 2s,2p states cover a broad band 2−10 eV below E_F. States 0−2 eV above E_F are dominated by C 2p and N s,p with some Ni 3d,4s,p, S 3p, and O 2p states appearing at the upper end of the range.

We thus see that all six peripherally substituted molecules have common spectral features, while differing in detail. As anticipated the metal and N "core" states are relatively little affected, compared to major shifts and restructuring of peaks localized on peripheral atoms and charge transfer bands discussed below. O s,p states are seen to be consistently more tightly bound than S s,p, consistent with O being a better electron acceptor, as already shown by the Mulliken charges of Table 1.

3. Molecular Orbital Structure. In simplified orbital models, it is usual to identify a few critical MOs and to represent optical transitions in terms of single particle transitions among them. The four-orbital $\pi \rightarrow \pi^*$ model for porphyrins (a_{1u}, a_{2u}) → (e_g) and phthalocyanines (a_{1u}, a_{2u}, b_{2u}) → (e_g) certainly has the advantage of simplicity and neatness.[14] Here the reduced-symmetry splitting of the 2-fold e_g final state provides a mechanism for the observed band splittings, as discussed in more detail below. We find, on the other hand, that quite a number of initial and final states contribute to the Q- and B-bands, and while the transitions postulated in the four-orbital model contribute, they do not appear to be really dominant. In order to maintain some contact with the orbital picture, and to give some quantitative measure of states appearing at the optical threshold, we give the HOMO and LUMO symmetry labels and energy levels in Table 2 along with atomic orbital contributions. The molecule 4PZ has the largest band gap, 1.86 eV, while the other D_{4h} molecule 4PC has a gap of 1.42 eV. We find that ligand substitutions reduce the gap. For 2:2, 1:3, and 3:1 cases, the band gaps are predicted to fall around 1.18−1.50 eV. From total DOS figures (Figure 2), one can see the band gap region for each molecule explicitly.

More complete data on MO atomic composition are visible in Figure 2 for a considerable energy range. It is clear that many levels lie within ±2 eV of E_F, and optical transitions will arise from a variety of dipole-allowed pairs and not just from HOMO−LUMO transitions. From a detailed MO symmetry analysis not given here we can infer that indeed many of the low-lying allowed transitions will be of $\pi \rightarrow \pi^*$ nature; moreover, they are quite mixed in atomic initial and final state character. Thus the detailed wave function analysis and oscillator strength calculation is needed in understanding intensities and band shifts.

C. Optical Absorption Spectra. We now make comparison of our theoretical optical transition energies and intensities with the experimental absorption in solution. Dipole-allowed electronic transitions are considered for the different symmetry groups. General features of the symmetry-related splittings can be understood in terms of the simple semiempirical four-orbital model.[13,14] According to this model, the Q-band transition in phthalocyanine macrocycles at ~680 nm is generally assigned to an $a_{1u} \rightarrow e_g$ ($\pi \rightarrow \pi^*$) transition, where the a_{1u} orbital has maximum electron density on the meso and pyrrole nitrogen atoms of the framework. In porphyrin macrocycles the Q-band is assigned to $a_{2u} \rightarrow e_g$ ($\pi \rightarrow \pi^*$) transitions. The Soret or B-band transition (~330 nm) in phthalocyanine is interpreted as due to $a_{2u} \rightarrow e_g$ transitions and in porphyrin macrocycles is considered to result from $a_{1u} \rightarrow e_g$ transitions. The $D_{4h} \rightarrow D_{2h}$, C_{2v} symmetry lowering would result in splitting of the degenerate e_g level, giving a natural interpretation of the double-peak structure seen experimentally. However, previous calculations[1,2] and the present work show that the MO structure is much richer, with significant contributions from ligand states falling within the infrared (IR), near-infrared (near-IR) and visible regions. In the following we will comment on similarities and differences between the semiempirical predictions and first-principles results.

The optical absorption spectra for six nickel porphyrazines calculated according to eqs 5 and 6 are compared with the experimental solution absorption spectra in Figure 3.

1. Q-Band Transitions. a. 4PZ. Experimental and calculated absorption spectra of 4PZ are shown in Figure 3a. In the visible region, the first strong (Q-band) absorption peak lies at 1.85 eV (672 nm) in the experimental spectra. A shoulder at ~2.0 eV is presumably vibronic in character. Our calculated spectrum shows a major in-plane transition $11b_{2g} \rightarrow 22e_u$ at

---

[14] Gouterman, M. In *The Porphyrins*; Dolphin, D., Ed.; Academic Press: New York, 1978; Vol. 2, Chapter 1.

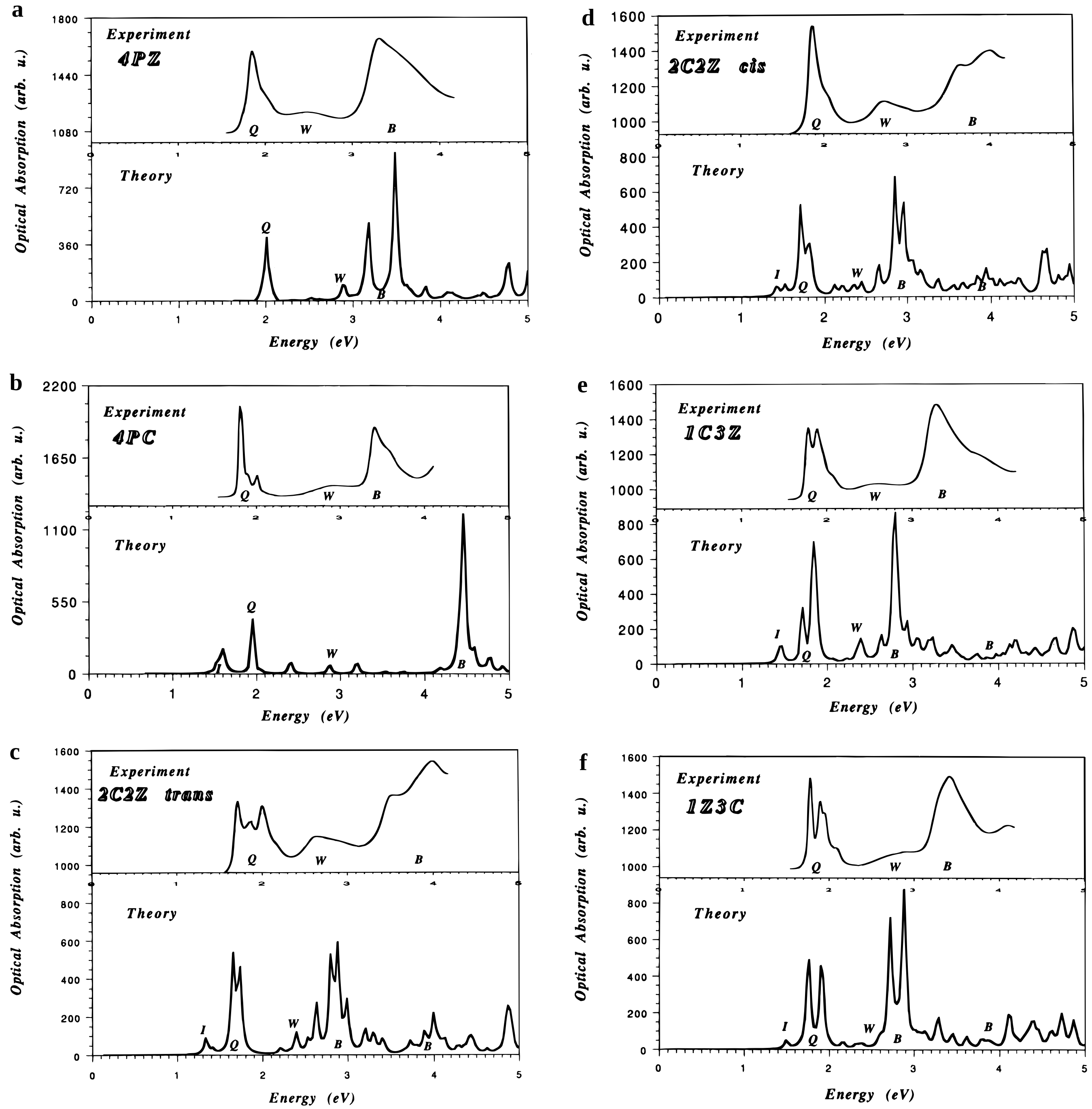

Figure 3. (a) Experimental and calculated optical absorption spectra of 4PZ. (b) Experimental and calculated optical absorption spectra of 4PC. (c) Experimental and calculated optical absorption spectra of 2C2Z trans. (d) Experimental and calculated optical absorption spectra of 2C2Z cis. (e) Experimental and calculated optical absorption spectra of 1C3Z. (f) Experimental and calculated optical absorption spectra of 1Z3C.

2.05 eV (606 nm) due to ligand to ligand charge transfer (LLCT) between pyrrole and meso nitrogens, plus C_a, C_b carbons. There is however, also a notable sulfur content in $11b_{2g}$ (14.8% S 3p and 1.1% S 3d) and $22e_u$ (28.0% S 3p and 13.2% S 3d), which shows the calculated transition to be of different atomic and symmetry character from the semiempirical $a_{2u} \rightarrow e_g$ $\pi \rightarrow \pi^*$ transition model. Nevertheless, the calculated peak position and its isolation from other features is in rather good agreement with experiment.

b. 4PC. Experimental and calculated absorption spectra of 4PC are shown in Figure 3b. In the Q-band region, the experimental spectrum shows a major peak Q at about 1.82 eV (683 nm). A vibrational side-band is seen at ~1.95 eV, and a third distinct weak-peak is also found near 2 eV (622 nm). In our calculations, a major in-plane transition $2a_{1u} \rightarrow 9e_g$ is found at 1.95 eV (637 nm) due to LLCT between carbons C_a, C_b, C_c, and C_d and oxygens. This is very similar to the $\pi \rightarrow \pi^*$ Q-band transition found in the Ni4C phthalocyanine.[1] A fairly strong $3b_{1u} \rightarrow 9e_g$ transition (I) predicted at 1.58 eV (787 nm) may belong to the near-infrared absorption, as will discussed later. Another possibility is that the $b_{1u} \rightarrow e_g$ and $a_{1u} \rightarrow e_g$ peaks are simply red-shifted with respect to the experimental peaks. However, the calculated relative intensities are not in agreement with experiment.

c. 2C2Z trans. Experimental and calculated absorption spectra of 2C2Z trans are shown in Figure 3c. For this D_{2h} molecule, the experimental spectrum in the Q-band region shows a splitting into two major peaks, one at 2.10 eV (592 nm) and the second at 1.73 eV (718 nm). The feature at 1.90 eV between these two major peaks, and the high-energy shoulder on the 2 eV peak may be vibrational sidebands. In our calculations, we also find two electronic dipole in-plane transitions contributing in the Q-band region. One is a $6a_u \rightarrow 9b_{3g}$ transition at 1.77 eV (702 nm) due mostly to the LLCT with some of the ligand to metal charge transfer (LMCT) character due to 6% Ni 3d in the final state. A second calculated transition $6a_u \rightarrow 9b_{2g}$ at 1.65 eV (753 nm) represents the other component of the symmetry-split $e_g \rightarrow b_{2g},b_{3g}$ final states with 10% Ni 3d contents. The calculated peak splitting of 0.12 eV is only about 1/3 that of experiment. The qualitative feature of e_g level splitting in D_{4h} to two levels (b_{2g}, b_{3g}) in D_{2h} is, however, verified in the numerical calculations, and the center of the band complex is in fairly good agreement with the experiment. As in the 4PC case discussed above, it is possible that the calculated weak IR band I (at 1.35 eV) is a red-shifted component of the Q-band. This would give very good agreement with the experimental splitting of 0.38 eV, consistent with the following cases; however, the disparity in intensities makes this interpretation dubious.

d. 2C2Z cis. Experimental and calculated absorption spectra of 2C2Z cis are shown in Figure 3d. One major peak at 1.85 eV (672 nm) and another weak peak or shoulder at about 2.00 eV (620 nm) are found in the experimental Q-band region. Our calculation shows one strong $\pi \rightarrow \pi^*$ in-plane transition $14a_2 \rightarrow 16a_2$ at about 1.72 eV (722 nm) dominated by LLCT with some small amount of LMCT (7% Ni 3d states in $16a_2$). A second weaker in-plane $\pi \rightarrow \pi^*$ transition $14a_2 \rightarrow 17b_1$ is predicted at 1.84 eV (676 nm) with similar final state orbital character. The calculated splitting of 0.12 eV here is in good agreement with experiment (0.15 eV). Predictably, a_2 and b_1 arise from the splitting of the e_g symmetry as in D_{4h} macrocycles. A weak IR band is predicted around 1.4−1.6 eV.

e. 1C3Z. Experimental and calculated optical absorption spectra of C_{2v} 1C3Z are shown in Figure 3e. Two well-separated peaks and a high energy shoulder are found in the experiment: at 1.80 eV (691 nm) , 1.91 eV (651 nm), and ∼2.05 eV (606 nm), respectively. The calculations show an in-plane $\pi \rightarrow \pi^*$ transition $13a_2 \rightarrow 15\ a_2$ at 1.73 eV (718 nm) dominated by LLCT with lesser LMCT features (9% Ni 3d in $13a_2$ and 7% Ni 3d in $15a_2$). A second, stronger, peak is due to the in-plane $\pi \rightarrow \pi^*$ transition $13a_2 \rightarrow 18b_1$ at 1.86 eV (668 nm), also dominated by LLCT with little LMCT character (7% Ni 3d in $18b_1$). This is also consistent with the expected a_2 and b_1 levels split from the e_g symmetry as in D_{4h} macrocycles. The calculated peak splitting of 0.13 eV is in good agreement with the experimental value of 0.11 eV. A weak IR band is again predicted ∼1.5 eV.

f. 1Z3C. Experimental and calculated absorption spectra of C_{2v} 1Z3C are shown in Figure 3f. Two well-defined peaks are found in experiment at 1.78 eV (698 nm) and 1.90 eV (654 nm) with a high energy shoulder ∼2.1 eV (592 nm). Our calculations show an in-plane $\pi \rightarrow \pi^*$ transition $14a_2 \rightarrow 15\ a_2$ at 1.75 eV (710 nm) dominated by LLCT with some weak LMCT character (9% Ni 3d in $15a_2$). The second peak is due to the in-plane $\pi \rightarrow \pi^*$ transition $14a_2 \rightarrow 18b_1$ at 1.92 eV (647 nm), with similar orbital character (7% Ni 3d in $18b_1$). Again here, the e_g final state is split into a_2 and b_1 components. The calculated peak splitting of 0.17 eV is in fair agreement with the experimental value of 0.12 eV, while a weak IR band is predicted at ∼1.5 eV.

A summary of experimental and calculated Q-band transitions, energies, and oscillator strengths is given in Table 3. We see that the overall discrepancy between theory and experimental band peaks is 0.1−0.2 eV, which is quite small considering the limitations of DF theory, use of ground state orbitals, estimated bond lengths, H-termination, etc. With the exception of 2C2Z trans, the symmetry-derived band splittings of 0.12−0.15eV are well reproduced by theory.

Table 3. Calculated and Experimental Q-Band Transitions (ϵ_{if} = Transition Energy; f = Theoretical Oscillator Strength), Where All Reported Transitions Have in-Plane Directional Character

	transition	ϵ_{if} (eV)		theory
system	symmetry-type	theory	experiment	f
4PZ	$11b_{2g} \rightarrow 22e_u$	2.05	1.85	0.88
4PC	$2a_{1u} \rightarrow 9e_g$	1.95	1.82	0.63
2C2Z trans	$6a_u \rightarrow 9b2_g$	1.65	1.70	1.04
	$\rightarrow 9b3g$	1.77	2.00	0.86
2C2Z cis	$14a_2 \rightarrow 16a_2$	1.72	1.85	1.58
	$\rightarrow 17b_1$	1.84	2.00	1.06
1C3Z	$13a_2 \rightarrow 15a_2$	1.73	1.80	1.26
	$\rightarrow 18b_1$	1.86	1.91	1.37
1Z3C	$14a_2 \rightarrow 15a_2$	1.75	1.78	1.67
	$\rightarrow 18b_1$	1.92	1.90	1.60

2. Higher Energy Band Transitions. The familiar Soret absorption band (B-band) found for a typical porphyrazine system falls around 3.80 eV (330 nm).[13,15] For the nickel-centered porphyrazines, the Soret bands are observed (Figure 3) over the range 3−4 eV. With O- and S-containing peripheral substituents, an additional band (called W in the following) appears around 2.5−2.6 eV (∼490 nm), which is usually considered as a $n \rightarrow \pi^*$ transition (n: non-bonding state of sulfur or oxygen), showing the strong electrodonating behavior of S and O.[16,17] Our calculations confirm and make quantitative this idea, showing significant C 2p character in addition to the expected strong O 2p and S 3p components. We now discuss the calculated Soret band and W band structures of each molecule in relation to the experimental absorption. It is well to note that the calculations presented here are all based upon the *ground state* potential and eigenvectors. As discussed earlier, for transitions between diffuse states with modest charge rearrangement, this is known to be a good approximation. However, for charge-transfer bands and other excitations which produce significant final state charge and/or geometric relaxation, it is clear that significant errors will result. Since our main emphasis here is upon understanding the low-lying Q-band structure, we will not pursue the question of final state effects in the B-bands. We will however, interpret the considerable band shifts seen in comparing calculated and measured B-bands as evidence for considerable relaxation, which would be interesting to treat in the future.

a. 4PZ. For 4PZ (Figure 3a), the experimental Soret band spans a region B around 3.0−4.0 eV, with a major peak at about 3.40 eV (366 nm). In our calculations, it is found that several transitions contribute to region B. The in-plane transitions $8e_g \rightarrow 9b_{1u}$ at 3.17 eV (392 nm) and $7e_g \rightarrow 9b_{1u}$ at 3.49 eV (357 nm) are primarily due to LLCT $\pi \rightarrow \pi^*$ transitions. Another weak transition $21e_u \rightarrow 10a_{1g}$ is located at 3.11 eV (400 nm). The agreement between theory and experiment is rather good.

Experimentally, the W band is located around 2.50 eV (497 nm). We find transitions $3a_{1u}$ (78% Ca,b 2p and 21% S 3p) $\rightarrow$ $10a_{2g}$ (68% Ca,b 2p, and 10% S 3p) at 2.86 eV (435 nm) and 23eu (35% S 3p) $\rightarrow 9e_g$ (4% N_p 2p, 21% N_m 2p, 7% C_b 2p, 8% S 3p) at 2.90 eV (429 nm) contributing to this band, showing that sulfur and carbons may donate nonbonding electrons to nitrogen 2p states or exchange electrons between themselves in this energy region.

---

(15) Velazquez, C. S.; Broderick, W. E.; Sabat, M.; Barrett, A. G. M.; Hoffman, B. M. *J. Am. Chem. Soc.* **1990**, *112*, 7408.

(16) Doppelt, P.; Huille, S. *New J. Chem.* **1990**, *14*, 607.

(17) Sibert, J. W.; Lange, S. J.; Stern, C. L.; Barret, A. G. M.; Hoffman, B. M. *Angew. Chem., Int. Ed. Engl.* **1995**, *34*, 2020.

b. 4PC. For 4PC (Figure 3b), the experimental Soret band of region B falls around 3.2−3.8 eV, with a major peak at about 3.46 eV (360 nm). The calculated spectra show the Soret band considerably blue-shifted (∼80 nm), consisting of $7e_g \rightarrow 5b_{2u}$ (4.45 eV, 279 nm), $3b_{1u} \rightarrow 10e_g$ (4.78 eV, 260 nm), and $7e_g \rightarrow 6a_{1u}$ (4.41 eV, 282 nm) contributing to the Soret band transitions in region B. These are all in-plane transitions, due to LLCT and some LMCT. The rather large discrepancy of ∼1 eV between experimental and theoretical B-band peaks invites further study of the relaxation processes involved.

The experimental spectra also show absorption in the W region (2.3−3.2 eV) corresponding to predicted weak transitions, such as $6e_g$ (89% C 2p and 12% O 2p) → $3a_{1u}$ (88% C 2p and 10% O 2p) at 2.41 eV (516 nm) and $25e_u$ (43% N 2p, 48% C 2p and 5% O 2p) → $13b_{1g}$ (34% N 2p, 52% C 2p and 2% O 2p) at 2.87 eV (433 nm). This shows that the W band is here mainly contributed by carbon and oxygen non-bonding electron exchange and some oxygen to nitrogen electron donation.

c. 2C2Z trans. For 2C2Z trans (Figure 3c), the experimental Soret band shows strong transitions with onset ∼3.3eV and peaks at 3.55 and 4.05 eV defining region B. The MO states responsible for this absorption, such as $8b_{1u} \rightarrow 9b_{2g}$ at 2.81 eV (442 nm), $8b_{1u} \rightarrow 9b_{3g}$ at 2.88 eV (432 nm) and $5a_u \rightarrow 9b_{3g}$ at 2.99 eV (416 nm) are in plane transitions of mostly LLCT and a small amount of LMCT in character. The calculated intensity of the B-band region is much too small, even including additional transitions, such as $7b_{2g} \rightarrow 10b_{1u}$, $6b_{2g} \rightarrow 10b_{1u}$, and $4a_u \rightarrow 9b_{3g}$ found around the 4eV (311 nm) region. The simplest interpretation of this result is that the entire theoretical B-band structure has been red-shifted by ∼0.5 eV, an amount quite typical of excited state relaxation seen in previous DF studies on porphyrines.

Some weak transitions observed in the W band (2.4−3.0 eV) can be interpreted in terms of transitions $9b_{1u}$ (69% S 3p) → $10b_{2g}$ (8% N 2p, 78% C 2p, 4% O 2p) at 2.21 eV (563 nm), $6a_u$ (59% S 3p and 3% O 2p) → 10 b_{2g} at 2.53 eV (492 nm), and $6a_u \rightarrow 26a_g$ (10% Ni 3d, 10% N 2p, 78% C 2p) at 2.62 eV (475 nm). This also shows mostly sulfur and some minor oxygen electron donation in W band transitions to nitrogen and carbon.

d. 2C2Z cis. For 2C2Z cis (Figure 3d), the experimental spectra show features similar to 2C2Z trans, in the region W and B from 2.1 to 4.6 eV. Our calculations show that the region W covering 2.1−2.7 eV and the region B covering 2.8−4.5 eV is dominated by $\pi \rightarrow \pi^*$ $13b_1 \rightarrow 16a_2$ at 2.86 eV (435 nm) and $13b_1 \rightarrow 17\ b_1$ at 2.96 eV (420 nm) transitions. LLCT and some lesser LMCT are responsible as expected for the B-band region 3.2−4.5 eV, including $12a_2 \rightarrow 17a_2$ and $12a_2 \rightarrow 18b_1$, where the calculated intensity is much too low. It is again plausible to interpret the results as a ∼0.5 eV red-shift of the calculated B-band due to omission of final state relaxation effects. There is a prominent calculated W band transition $15a_2$ (12% Ni 3d, 52% S 3p and 32% C 2p) → $19b_1$ (20% N 2p, 42% C 2p, 5% S 3p and 6% O 2p) at 2.65 eV (469 nm), showing sulfur electron transfer to nitrogen and carbon.

e. 1C3Z. For 1C3Z (Figure 3e), the experimental Soret band is located around 3.2−3.8 eV (∼370 nm) and the feature W (∼2.6 eV) returns to low intensity. Our calculations show that the major Soret band is again red-shifted about 78 nm, and that $14b_1 \rightarrow 15a_2$ at 2.78 eV (447 nm) and $14b_1 \rightarrow 18b_1$ at 2.81 eV (442 nm) make a major contribution to the Soret band with LLCT and some LMCT. Some additional weak transitions, such as $16b_1 \rightarrow 20b_1$, $17b_1 \rightarrow 20b_1$, and $14a_2 \rightarrow 21b_1$ are found in region B to higher energy.

Our calculated W band at ∼2.3−2.6 eV shows a major transition $15b_1$ (19% Ni 3d, 44% S 3p and 2% O 2p) → $15a_2$ (7% Ni 3d, 27% N 2p and 62% C 2p) at 2.39 eV (520 nm), with charge transfer from sulfur to the pyrrole core and also some transfer to just inside the core region.

Table 4. Calculated and Experimental Soret Band (B-Band) Transitions (ϵ_{if} = Transition Energy; f = Theoretical Oscillator Strength)

system	transition symmetry-type	ϵ_{if} (eV) theory	ϵ_{if} (eV) experiment	theory f
4PZ	$21e_u \rightarrow 10a_{1g}$	3.11	∼3.40	0.14
	$8e_g \rightarrow 9b_{1u}$	3.17		0.80
	$7e_g \rightarrow 9b_{1u}$	3.49		1.85
4PC	$7e_g \rightarrow 6a_{1u}$	4.41	∼3.46	0.68
	$7e_g \rightarrow 5b_{2u}$	4.45		0.83
	$3b_{1u} \rightarrow 10e_g$	4.78		0.38
2C2Z trans	$8b_{1u} \rightarrow 9b_{2g}$	2.81	∼3.55	1.06
	$5a_{2u} \rightarrow 9b_{3g}$	2.99	∼4.05	0.58
	$4a_u \rightarrow 9b_{3g}$	4.00		0.17
2C2Z cis	$13b_1 \rightarrow 16a_2$	2.86	∼3.65	1.78
	$\rightarrow 17b_1$	2.96	∼4.05	1.59
	$12a_2 \rightarrow 17a_2$	3.96		0.15
1C3Z	$14b_1 \rightarrow 15a_2$	2.78	∼3.32	1.84
	$\rightarrow 18b_1$	2.81		1.57
	$16b_1 \rightarrow 20b_1$	4.16		0.20
1Z3C	$15b_1 \rightarrow 15a_2$	2.72	∼3.40	2.13
	$\rightarrow 18b_1$	2.78	∼4.08	1.98
	$14b_1 \rightarrow 16a_2$	4.12		0.49

f. 1Z3C. For 1Z3C (Figure 3f), the experimental Soret band falls around 3.2−3.8 eV (∼370 nm) and the low intensity region W falls around 2.4−3.0 eV. Our calculation shows a ∼0.5 eV red-shifted Soret band, with major transitions $15b_1 \rightarrow 15\ a_2$ at 2.72 eV (457 nm) and $15b_1 \rightarrow 18\ b_1$ at 2.88 eV (432 nm), due to the in plane LLCT and some LMCT. Some weak transitions are also obtained to higher energy in region B (∼4.0 eV).

The calculated W band is not very well resolved, since it is strongly overlapped by the B band. There are some weak peaks around the 2.60 eV region, such as $15b_1$ (79% N 2p, 11% C 2p, S 3p 2% and 7% O 2p) → $14a_2$ (15% N 2p, 82% C 2p and 3% O 2p) at 2.62 eV (476 nm) which demonstrate the LLCT nature of the W band.

A summary of experimental and selected calculated Soret band transitions with the largest intensity, energies, and oscillator strengths is given in Table 4.

3. IR or Near-IR Transitions. No experimental data are available as yet in the infrared (IR) and near-infrared (near-IR) absorption regions for these porphyrazines. Our calculations predict some IR or near-IR transitions for these compounds (region I in Figure 3), which we now discuss.

The band gap in 4PZ is so large (1.86 eV) that we do not expect any electronic IR transitions. For 4PC, we found a fairly strong LLCT $3b_{1u} \rightarrow 9e_g$ near-IR transition at 1.58 eV (787 nm); as mentioned above, it is possible that this is a red-shifted component of the Q band. The band gaps in D_{2h} and C_{2v} macrocycles are reduced to ∼1.45 eV, so we predict some IR or near-IR transitions for 2C2Z trans ($9b_{1u} \rightarrow 9b_{2g}$, 1.36 eV, 914 nm), 2C2Z cis ($16b_1 \rightarrow 16a_2$, 1.43 eV, 869 nm), 1C3Z ($14a_2 \rightarrow 15a_2$, 1.43 eV, 869 nm), 1Z3C ($17b_1 \rightarrow 15a_2$, 1.50 eV, 829 nm). They are all in-plane transitions, dominated by LLCT and some of lesser LMCT character. The intensity of these bands is predicted to be quite low.

IV. Conclusions

The self-consistent atomic configurations show that ligand substitution introduces most significant changes nearby the substitution sites. A band-gap varying from 1.20 to 1.87 eV has been predicted for these nickel porphyrazines, with lower symmetry compounds displaying lower HOMO−LUMO gaps.

The intensity of low-lying transitions was determined by considering the dipole selection rules and the oscillator strengths. Major peaks match the experimental Q-band rather well. The transition dipoles lie mostly in the molecular plane for both Q- and B- band absorption. Some so-far unmeasured infrared and near-infrared transitions have been predicted and may be of interest once crystalline specimens have been obtained.

For the high symmetry D_{4h} 4PZ and 4PC macrocycles, the single-peak Q band and Soret band transitions are basically of LLCT character, with the transition moment lying in the molecular plane. The calculated Soret band of the 4PC macrocycle is blue-shifted about 80 nm compared to experiment, indicating the magnitude of final state charge transfer effects on the potential. For the lower symmetry D_{2h} 2C2Z trans compound, the e_g final state is split as expected into b_{2g} and b_{3g} components. The LLCT transitions are still dominant but we also find some lesser LMCT character. The C_{2v} macrocyles 2C2Z cis, 1C3Z, and 1Z3C have some common properties in the Q-band transition: The transition peak is split into two $\pi \rightarrow \pi^*$ transitions. One component is $a_2 \rightarrow a_2$ and the other is of $a_2 \rightarrow b_1$ symmetry derived from the final state $e_g \rightarrow (a_2, b_{1)}$ symmetry splitting, again basically dominated by LLCT, with some lesser LMCT. The calculated Soret bands for the C_{2v} systems are red-shifted (in the ground state potential) by about 88 nm compared to experiment.

Comparing our theoretical results with experiment, we have put forward a detailed picture of the effective atomic configurations and optical absorption schemes. The Q-bands are rather well described, while a systematic red-shift of ~0.5 eV is noted for predicted B-band absorption in the low symmetry macrocycles. The W-band absorption as found in experiment is mainly contributed by charge transfer from sulfur or oxygen ligands to the core region and its immediate periphery, consistent with expectations. We suspect that the exceptionally good agreement between theory and experiment for the 4PZ case in Q-, W-, and B-bands is fortuitous.

Discrepancies between our theoretical model and experiment may be due to a variety of factors, including the following:(1) assumed interatomic distances not considering excited state and ligand substitution relaxation effects (including solvent effects); (2) H termination; i.e. substitution of distant terminal groups ($-(CH_2CH_2O)_3H$ in star-porphyrazine and $-(CH_2)_7CH_3$ in the phthalocyanine macrocycle) with hydrogen atoms; (3) use of DF ground state orbitals and potential in predicting excitations; (4) limitations of a small basis optimized for the ground state; (5) fundamental limitations of DF theory in describing excited state phenomena.

Limitations 1−4 may be removed by more extensive calculations; additional experimental structural and spectroscopic data would be useful. The simultaneous treatment of geometric and electronic relaxation in excited states can perhaps be treated in the future by so-called Born−Oppenheimer DF molecular dynamics methods.

Acknowledgment. This work is supported by the MRL Program of the National Science Foundation, at the Materials Research Center of Northwestern University, under Award No. DMR-9120521. Calculations were carried out in part at the National Center for Supercomputer Applications at the University of Illinois at Urbana-Champaign.

IC960005Q